European Radiology (2019) 29:7009–7018
https://doi.org/10.1007/s00330-019-06287-5

HEAD AND NECK

The growing concern of radiation dose in paediatric dental and maxillofacial CBCT: an easy guide for daily practice

Andreas Stratis[1,2] · Guozhi Zhang[2] · Reinhilde Jacobs[1] · Ria Bogaerts[2] · Hilde Bosmans[2]

Received: 15 September 2018 / Revised: 21 April 2019 / Accepted: 24 May 2019 / Published online: 1 July 2019

Abstract

Objectives To provide an indication-based and scanner-specific radiation dose and risk guide for paediatric patients undergoing dental and maxillofacial cone beam computed tomography (CBCT) examinations.

Methods Five commercially available scanners were simulated in EGSnrc Monte Carlo (MC) code. Dedicated, in-house built, head and neck voxel models, each consisting of 22 segmented organs, were used in the study. Organ doses and life attributable risk (LAR) for cancer incidence were assessed for males and females, aged 5 to 14 years old, for every clinically available protocol: central upper and lower incisors, upper and lower premolars, upper and lower jaws, cleft palate, temporal bone, sinus, dentomaxillofacial complex, and face and skull imaging. Dose results were normalised to the x-ray tube load (mAs) and logarithmic curves were fit to organ dose and risk versus age data.

Results Females demonstrated higher LAR values in all cases. A well-established dose decreasing pattern with increasing age-at-exposure was observed. Central upper incisor protocols were those with the lowest risk, contrary to skull protocols which provided the highest LAR values. Salivary glands and oral mucosa were the highest irradiated organs in all cases, followed by extrathoracic tissue (ET) in protocols where the entire nasal cavity was inside the primary field. The dose to thyroid was considerably high for younger patients.

Conclusions This work provides an extensive dose assessment guide for 5 dental CBCTs, enabling detailed dose assessment for every paediatric patient.

Key Points

- *Radiation dose concerns due to the growing use of paediatric dental and maxillofacial CBCT underline the need for justification that should in part be based on radiation exposure in radiology.*
- *Patient-specific dose calculations based on Monte Carlo simulations and head-neck paediatric voxel models overcome the limitations of conventional thermoluminescent dosimeter (TLD) dosimetry and provide proper guidance for justification of CBCT exposures.*
- *Monte Carlo simulations with head-neck models reveal an organ dose and radiation risk decreasing pattern with increasing age at exposure, and with decreasing size of the scanning volume of interest (field of view).*

Keywords Cone beam computed tomography · Radiation dosage · Child · Head · X-rays

Andreas Stratis and Hilde Bosmans equally contributed to this work.

Electronic supplementary material The online version of this article (https://doi.org/10.1007/s00330-019-06287-5) contains supplementary material, which is available to authorized users.

✉ Andreas Stratis
andreas.stratis@uzleuven.be

[1] Katholieke Universiteit Leuven, Department of Imaging and Pathology, OMFS-IMPATH Research Group, Campus St. Rafael, Kapucijnenvoer 33, Leuven 3000, Belgium

[2] University Hospitals of Leuven, Department of Radiology, Herestraat 49, Leuven 3000, Belgium

Abbreviations

μGy	Microgray
2D	Two-dimensional
3D	Three-dimensional
CBCT	Cone beam computed tomography
CLI	Central lower incisors
CUI	Central upper incisors
CV	Coefficient of variance
ED	Effective dose
ET	Extrathoracic tissue
FOV	Field of view
LAR	Life attributable risk
LJ	Lower jaw
mAs	Milli ampere second product
MC	Monte Carlo
MDCT	Multi-detector computed tomography
PL	Lower premolar
PU	Upper premolar
RBM	Red bone marrow
SAD	Source to axis of rotation distance
SDD	Source to detector distance
Sv	Sievert
TCM	Tube current modulation
TLD	Thermoluminescent dosimeter
ULJ	Upper and lower jaw

Introduction

The introduction of cone beam computed tomography (CBCT) in early 2000 gave a new perspective in head and neck 3D imaging due to the widespread range of applications and high image quality, and also to low cost, small size, and limited medico-legal requirements [1–4]. CBCT imaging gradually replaced dental MDCT and 2D panoramic acquisitions without always presenting a sound evidence for the added value in terms of the diagnostic outcome. Organisation bodies and scientific groups have worked over the last years towards developing a justification frame [5–10]. However, the growing concern is not only related to increasing use of CBCTs but also to the radiation dose of each CBCT, which is not insignificant.

As published by the Health Protection Agency (UK), the dose to a patient in a dental CBCT scan is generally lower compared with that in dental MDCT exposures, but it is still 2–45 times higher than 2D panoramic acquisitions [8]. Besides, and based on the same reference, there are overlapping values in CBCT and MDCT doses. Dose reduction techniques in state-of-the-art MDCT scanners, such as tube current modulation (TCM), iterative reconstruction (IR), and adaptive collimation, have reduced MDCT doses to CBCT levels, reaching effective dose (ED) values of 180 μSv for oral implant and maxillofacial surgery planning and 280 μSv for temporal bone imaging [11, 12]. A recent meta-analysis of published data showed that adult ED in dental CBCT imaging ranges from 5 to 622 μSv for small FOVs (7–521 μSv for children), 9–560 μSv for medium FOVs (13–769 μSv for children), and 46–1073 μSv for large FOVs (13–769 μSv for children) [13]. The most remarkable feature is the reported ranges among different machines. Pauwels et al have reported a 19-fold dose range for 14 CBCT models, Ludlow et al a 16-fold range for 7 CBCT scanners, and Rottke et al a 23-fold range for 10 CBCT scanners [14–16].

Most CBCT dose studies in the literature have been performed using thermoluminescent dosimeters (TLDs) mounted into anthropomorphic phantoms. TLD dosimetry, however, exhibits several limitations in CBCT imaging. Most importantly, currently available anthropomorphic phantoms do not represent the realistic anatomy of the head and neck region, since radiosensitive organs like salivary glands, oral mucosa, extrathoracic tissue (ET), oesophagus, and thyroid are not present. The delineation of these tissues in a physical anthropomorphic phantom depends on the experience of the user drawing these organs in the model, and hence dose results become very subjective. Furthermore, organ dose assessment is performed in a rather limited region of each organ. In conjunction with the fact that CBCTs present steep dose gradient and axial inhomogeneity [17], the partial irradiation of TLDs makes the results questionable.

In children, dose assessment is even more challenging. Organ doses depend on the fraction of the organ that is directly exposed to the primary radiation field. While adult organs do not vary in size and mass with age, this is not the case for children, putting even more stress on proper segmentation. In addition, children cannot be represented by a single anthropomorphic phantom and not even by 2 phantoms, one mimicking 5-year-old and another 10-year-old, as often performed in practice [18–20].

This work aims to overcome the above-mentioned limitations of conventional dosimetry and to provide an indication-oriented and scanner-specific radiation dose and risk guide for the entire age range in children. Radiation risk was assessed via both ED, using the ICRP publication 103 weighting factors [21], and life attributable risk (LAR). ED represents a gender-neutral and age-independent stochastic risk index, while LAR is a more precise gender and age-at-exposure-specific radiation risk metric. Even if ED has been criticised by the scientific community and is not applicable for paediatric population, it is still used by medical teams to evaluate the potential detriment of an exposure [22, 23].

Materials and methods

Monte Carlo framework and simulated CBCT scanners

An EGSnrc-based Monte Carlo (MC) framework was previously developed, calibrated and validated in our group [12, 24–27]. It consists of three individual components: source modelling, angular projection modelling, and dose tracking. The x-ray source modelling is based on the equivalent source model concept (ESM); this method has been introduced to obviate the need for obtaining proprietary data from vendors, required for the accurate simulation of the x-ray tube [28]. The ESM is part of the scanner and protocol–specific input file to the main source code which also incorporates the scanner geometric specifications and detailed information about the protocol that needs to be simulated: the SAD, the SDD, the FOV dimension, the x-ray tube projection angular intervals, the x-ray beam shape, the bowtie filter, the rotation angle, the Beam-On and Beam-Off angles, and the features of the (patient-specific) TCM curve. The dose tracking part is performed with a history-by-history statistical estimator; each simulated particle is tracked until it exits the geometry of interest or reaches the predefined cut-off energies, set at 10 keV for photons and 520 keV for electrons (9 keV of kinetic energy). Target simulation uncertainty on the dose is set to 99.7% confidence intervals [29, 30].

Five commercially available dental CBCT scanners were simulated in the study: Promax 3D Max (Planmeca), Accuitomo 170 (Morita), CS 9300 (Carestream), NewTom VGi evo, and NewTom 5G (QR srl). The technical specifications of each simulated scanner are listed in Table 1. The MC framework has been calibrated and validated for every clinically available protocol-FOV [25].

Paediatric voxel models

A paediatric head and neck voxel model database has been previously developed in our group and has been made, on request, available to the scientific community [31]. Each voxel model consists of 22 organs. The skin has been segmented as a one-voxel thick outline of the head and neck region. The sinuses, bone-skeletal mixture, mandible, and teeth were all segmented in a semiautomatic way by thresholding the grey values of these organs. The blood (arteries), brain, cartilage, connective tissue, oesophagus, eyes, eye lenses, fat, muscle, ET, spinal cord, tongue, trachea, thyroid, salivary glands, oral mucosa, and residual tissue were all segmented manually by delineating each organ on an image-by-image basis. The spongiosa and the cortical bone were segmented as a uniform bone-skeletal mixture. The resolution of most CT scanners nowadays is not adequate to allow for the segmentation of the medullary cavities where the red bone marrow (RBM) resides. The dose to RBM along with the dose to the radiosensitive bone surface and to lymph nodes can be assessed in an indirect way, applying mathematical formulas to the dose received by substitute organs [15, 32, 33].

Each organ mass was specified by multiplying the number of segmented voxels by the voxel volume and the respective organ density obtained from ICRP publication 110 and was compared and adjusted to the respective reference mass value published in ICRP publication 89 [34–36]. Twelve voxel models were used in the study covering the age from 5 to 14 years old. Their pseudonymised naming, age, gender, and their technical specifications are illustrated in Table 2.

Clinical protocols

For each voxel model and scanner, organ doses were calculated for the most common clinical indications: four tooth imaging cases (central upper incisors (CUI), central lower incisors (CLI), premolar upper (PU), and premolar lower (PL)), upper and lower jaw imaging (ULJ), lower jaw (LJ), and cleft palate imaging, sinus and dentomaxillofacial complex imaging, and face and skull imaging. For NewTom 5G, which is the only MDCT-like

Table 1 Technical specifications of dental CBCT scanners in the study

Scanner	Operating voltage (kV)	Bowtie filter	Rotation angle (°)	TCM	Cu filter	Offset acquisition
Promax 3D Max (Planmeca)	96 (1)	No	210/360 (3)	No	Yes	No (5)
Accuitomo 170 (Morita)	90 (1)	Yes	180/360 (4)	No	No	No
CS 9300 (Carestream)	70–90 (2)	Yes	200/360 (3)	No	Yes	No
NewTom 5G (QR S.R.L)	110	No	360	Yes	No	Yes
NewTom VGi-evo (QR S.R.L)	110	No	360	Yes	No	Yes

(1) The operating voltage can be altered by the user, yet the preset clinical protocols are carried out with the tube voltages indicated in the Table. (2) Depending on the FOV, the operation mode, and the size of the patient, the voltage varies from 70 to 90 kV. (3) In Promax 3D Max, for every clinical FOV apart from the largest one for skull imaging (23×16 cm^2 and 23×26 cm^2), the scanner employs a partial rotation (210°); for skull protocols, the rotation is 360°. In CS 9300, the rotation angle is 200° apart from the largest 17×13 cm^2 FOV. (4) Accuitomo 170 provides half and full rotation options for every FOV, yet only FOVs with 360° are applied in the clinic. (5) For every clinical FOV, apart from the largest one for skull imaging (23×16 cm^2 and 23×26 cm^2), the in-plane radiation field is symmetrical

Table 2 Specifications of the voxel models

Voxel model	Gender	Age (years)	In-plane resolution (mm)	*z*-resolution (mm)	*x*, *y* number of voxels	Number of slices	Head circumference (cm)
Dejan	Males	5	0.22	2.75	1024	60	50.5
Joris		6	0.49	1.95	512	108	52.1
Guozhi		7	0.21	3	1024	64	51.4
Peter		8	0.62	0.7	512	330	51.3
Benjamin		9	0.43	0.6	512	370	50.8
Andrew		10	0.49	0.6	512	342	53.7
Mike		12	0.49	2	512	126	52.3
Demi	Females	5	0.41	0.6	512	355	49.2
Xoch		8	0.49	3	512	76	52.2
Louisa		10	0.45	0.7	512	305	50.2
Vivian		12	0.41	1	512	230	51.8
Georgia		14	0.49	2.05	512	113	55.8

scanner with patients in a supine position laying on a table, organ doses were also calculated for monolateral and bilateral temporal bone imaging. The choice of the FOV for each clinical indication was based on the size of the head voxel model and on morphometric characteristics, in full accordance with the selection of the FOV in clinical practice.

For tooth imaging protocols, the selected small FOV was large enough to image a single tooth for the entire paediatric age range. For ULJ imaging, the rational of FOV selection was based on the clinical need that the scanning volume should encompass both jaws, i.e. the FOV diameter should be larger than the bigonial breadth, and the height larger than the menton-subnasal length. For LJ and cleft protocols, the bigonial breadth and the half menton-subnasal length (lower half for LJ and upper half for cleft) were used to specify the most appropriate FOV. For the maxillofacial complex and sinus protocols, the diameter of the selected FOV should be larger than the bizygomatic breadth, while the height of the FOV should be larger than the menton-nasal root length (or at least from gnathion to glabella) in the former protocols and such that it covers the distance from the lower edge of the maxillary sinus to the top of the frontal sinus for the latter protocols. The facial FOVs were picked such that they cover most of the facial anatomy whereas the skull protocols should fit the entire head from menton to the crown of the head. Figure 1 illustrates the facial morphometrics which guided

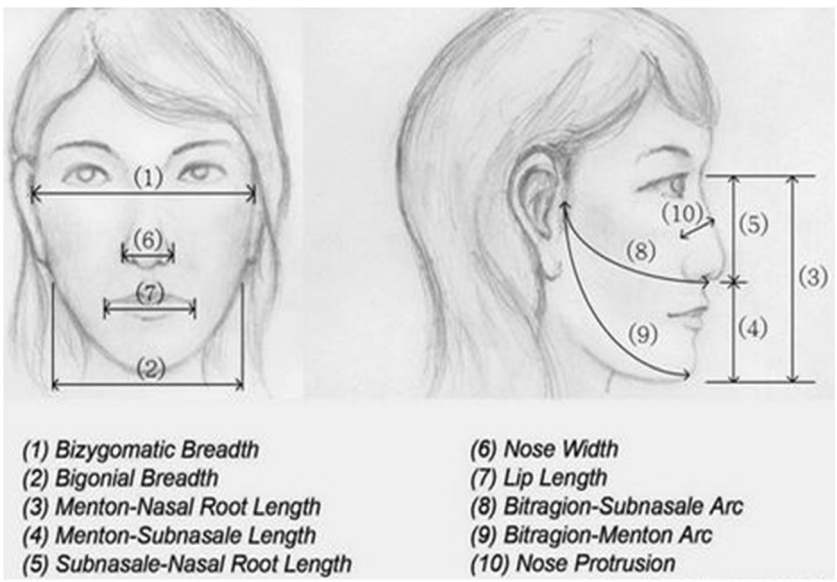

Fig. 1 Facial morphometrics for FOV selection

the FOV selection and Table 3 depicts the selected FOVs at each scanner for every protocol and voxel model.

Dose and risk calculations

While three of the simulated scanners allow the user to manually select the voltage (kV) of each protocol (Promax 3D Max, Accuitomo 170, CS 9300), only preset protocols by vendors at the time of installation, operating at a fixed voltage, are usually applied in daily routine (Table 1). Each protocol-FOV is clinically available in several operation modes. Dose-wise, the only difference between each operation mode is the total mAs/rotation. Therefore, in present work, organ dose and radiation risk values were normalised to mAs, to allow the reader to obtain absolute dose values once the mAs/rotation of the operation mode of interest is known and multiplied with the (normalised) dose conversion factor. ED and LAR incidence were calculated, and dose values were plotted as a function of age to enable dosimetric interpolations for those ages for which simulations were not performed.

The ultimate target of this work was to test whether there is any scanner and protocol-specific correlation between organ dose and radiation risk values versus age. A thorough analysis was carried out to investigate the correlation of organ dose, ED, and LAR patterns with age. To this end, individual organ doses were plotted against age, for each scanner and protocol, and a mathematical curve fit that provided a coefficient of determination (R^2) higher than 0.9 in all cases was selected. The Pearson correlation coefficient was also calculated. For those paediatric ages for which both males and females were simulated, sex-averaged organ dose values were calculated and included in the curve fitting analysis. The same applies to the ED vs age analysis. For LAR incidence, male and female dose values were analysed separately.

Each case was simulated in 1° angular steps with ten million histories per projection. The particle transport simulation was carried out with spin effects, electron impact ionisation, bound Compton scattering, radiative Compton corrections, atomic relaxations, and Rayleigh scattering all turned on. NRC Bremsstrahlung cross sections and the XCOM photon cross sections were employed.

Results

The number of simulated histories resulted in an MC simulation uncertainty, in terms of coefficient of variance (CV) of less than 0.5% in all radiosensitive organ doses. At first, for each individual organ, the average absorbed dose for a given clinical protocol and voxel model was calculated among all scanners. Data analysis revealed a poor correlation between protocol-specific absorbed organ dose values (for all scanners) with age (Pearson correlation coefficient range, − 0.35 to 0.12), mainly due to different acquisition geometries and energy spectra among scanners resulting in different dose distributions within the head. Subsequently, a scanner-specific analysis was conducted. Analysing each clinical case separately for each scanner, a very well-established organ dose decrease pattern with age was observed. The best fit option for organ doses, ED, and LAR incidence vs age was in all cases a logarithmic curve, following Eq. 1:

$$y = a \times \ln(x) + b \quad (1)$$

where y is the normalised absorbed organ dose value (μGy/mAs), the normalised ED (μSv/mAs), or the normalised LAR incidence (cases/100,000/mAs) and x is the age of the patient (in years). The values of a and b for every organ, and scanner, for the two most commonly applied clinical protocols, i.e. CUI and ULJ, along with each coefficient of determination (R^2) and Pearson correlation coefficient (r), are provided in Tables 4 and 5. Respective data for the other protocols are provided in Supplementary Tables 1–11.

Discussion

In this work, an extensive simulation study was set up to allow detailed radiation organ dose and risk analyses for the most common protocols in paediatric dental and maxillofacial CBCT imaging. Organ dose, effective dose, and life attributable cancer incidence risk were derived and tabulated. We have chosen to normalise these factors to mAs, rather than tabulating absolute values, since CBCT vendors use different operation-mode names to specify resolution levels. Naming has not been standardised among scanners. As an example, in terms of image quality, an 'ultra-low dose – normal reconstruction' mode in one vendor is close to a 'standard resolution' mode in another. Besides, for most CBCT scanners in the market, the only change is the x-ray tube loading (mAs), among different resolution-operation modes of a particular-FOV-protocol. Therefore, instead of tabulating absolute dose values that may not correspond to similar image resolution levels, this study presents normalised data, allowing the user to get absolute organ dose and risk values for a specific age, scanner, and protocol. This is obtained by calculating the normalised dose/risk from the tabulated factors (Tables 4 and 5, Supplementary Tables 1–11) and Eq. 1 and then multiplying the mAs of a specific protocol-operation mode of interest with the calculated normalised values. For instance, in a theoretical scenario where the user wants to estimate the dose to salivary glands and the ED for an 8-year-old that has undergone a 'regular' mode—upper and lower jaw protocol with NewTom Vgi-evo (110 kV, 10 mAs)—the calculations are

Table 3 The simulated clinical protocols

Protocol	Scanner	Voxel models		
		5–6 years old	7–11 years old	12–15 years old
Small FOVs (diameter × height, cm^2)				
Single tooth	Promax 3D Max	5 × 5.5	5 × 5.5	5 × 5.5
(CUI, CLI, PL, PU)	Accuitomo 170	6 × 6	6 × 6	6 × 6
	CS 9300*	5 × 5	5 × 5	5 × 5
	NewTom 5G**	6 × 6	6 × 6	6 × 6
	NewTom VGi evo**	5 × 5	5 × 5	5 × 5
Medium FOVs (diameter × height, cm^2)				
Lower jaw (LJ)	Promax 3D Max	8.5 × 4.8	10 × 5.5	10 × 5.5
	Accuitomo 170	10 × 5	10 × 5	10 × 5
	CS 9300*	10 × 5	10 × 5	10 × 5
	NewTom 5G**	8 × 8	12 × 8	12 × 8
	NewTom VGi evo**	8 × 5	10 × 5	10 × 5
Cleft	Promax 3D Max	8.5 × 4.8	10 × 5.5	10 × 5.5
	Accuitomo 170	10 × 5	10 × 5	10 × 5
	CS 9300*	10 × 5	10 × 5	10 × 5
	NewTom 5G**	8 × 8	12 × 8	12 × 8
	NewTom VGi evo**	8 × 5	10 × 5	10 × 5
Upper/lower jaw (ULJ)	Promax 3D Max	8.5 × 7.5	10 × 9	10 × 9
	Accuitomo 170	8 × 8	10 × 10	10 × 10
	CS 9300*	8 × 8	10 × 10	10 × 10
	NewTom 5G**	8 × 8	12 × 8	12 × 8
	NewTom VGi evo**	8 × 8	10 × 10	10 × 10
Monolateral temporal (MT)	Promax 3D Max	–	–	–
	Accuitomo 170	–	–	–
	CS 9300	–	–	–
	NewTom 5G**	8 × 8	8 × 8	8 × 8
	NewTom VGi evo**	–	–	–
Bilateral temporal (BT)	Promax 3D Max	–	–	–
	Accuitomo 170	–	–	–
	CS 9300	–	–	–
	NewTom 5G**	15 × 5	15 × 5	15 × 5
	NewTom VGi evo**	–	–	–
Large FOVs (diameter × height, cm^2)				
Maxillofacial complex	Promax 3D Max	10 × 9	10 × 13	10 × 13
	Accuitomo 170	10 × 10	10 × 10	10 × 10
	CS 9300	10 × 10	10 × 10	10 × 10
	NewTom 5G**	12 × 8	12 × 8	12 × 8
	NewTom VGi evo**	10 × 10	10 × 10	10 × 10
Sinus	Promax 3D Max	10 × 9	10 × 13	10 × 13
	Accuitomo 170	10 × 10	10 × 10	10 × 10
	CS 9300	10 × 10	10 × 10	10 × 10
	NewTom 5G**	12 × 8	12 × 8	12 × 8
	NewTom VGi evo**	10 × 10	10 × 10	10 × 10
Face	Promax 3D Max	13 × 13	13 × 13	13 × 16
	Accuitomo 170	14 × 10	14 × 10	17 × 12
	CS 9300	17 × 11	17 × 11	17 × 13.5
	NewTom 5G**	15 × 12	15 × 12	18 × 16
	NewTom VGi evo**	15 × 12	15 × 12	16 × 16
Skull	Promax 3D Max	23 × 26	23 × 26	23 × 26
	Accuitomo 170	17 × 12	17 × 12	17 × 12
	CS 9300	17 × 13.5	17 × 13.5	17 × 13.5
	NewTom 5G**	18 × 16	18 × 16	18 × 16
	NewTom VGi evo**	24 × 19	24 × 19	24 × 19

*CS 9300 operates at 80 kV for small FOV protocols and at 85 kV for medium and large FOV protocols

**Normal operation mode

Table 4 Central upper incisor (CUI) logarithmic curve parameters for organ doses, E, and LAR incidence (males and females) for all scanners

Scanner	Parameter	Brain	Skin	Oesophagus	Eye lens	Muscles	ET	Thyroid	Salivary glands	Oral mucosa	RBM	Bone surface	Lymph nodes	ED (μSv/mAs)	LAR incidence males	LAR incidence females
Promax 3D Max	*r*	−0.99	−0.98	−0.98	−0.97	−0.96	−0.99	−0.97	−0.95	−0.98	−0.89	−0.92	−0.96	−0.96	−0.97	−0.97
	R^2	0.974	0.991	0.961	0.936	0.953	0.983	0.960	0.958	0.986	0.901	0.923	0.922	0.980	0.989	0.991
	b	2.804	3.146	3.452	7.809	3.020	21.042	5.423	63.886	79.362	3.139	15.551	2.597	2.486	0.094	0.134
	a	−0.548	−0.73	−1.216	−2.082	−0.923	−6.158	−1.665	−16.03	−16.82	−0.966	−5.009	−0.079	−0.645	−0.03	−0.043
Accuitomo 170	r	−0.99	−0.99	−0.97	−0.94	−0.99	−0.94	−0.99	−0.93	−0.92	−0.98	−0.99	−0.98	−0.99	−0.99	−0.98
	R^2	0.92	0.96	0.95	0.94	0.97	0.94	0.96	0.94	0.95	0.92	0.97	0.89	0.98	0.99	1.00
	b	1.063	3.552	1.852	6.569	2.293	12.941	5.362	46.074	62.819	2.044	10.094	4.374	1.675	0.060	0.088
	a	−0.257	−0.923	−0.593	−1.522	−0.712	−3.875	−1.626	−12.38	−16.41	−0.581	−2.958	−1.129	−0.432	−0.019	−0.028
CS 9300	*r*	−0.94	−0.98	−0.98	−0.99	−0.99	−0.98	−0.99	−0.96	−0.99	−0.99	−0.99	−0.98	−0.99	−0.99	−0.99
	R^2	0.92	0.90	0.91	0.95	0.99	0.90	0.96	0.91	0.96	0.99	0.99	0.91	0.96	1.00	1.00
	b	0.352	1.808	0.570	4.077	0.585	5.036	2.384	4.717	49.932	0.845	3.919	2.470	0.850	0.033	0.051
	a	−0.055	−0.471	−0.182	−0.918	−0.173	−1.383	−0.694	−1.128	−10.14	−0.241	−1.119	−0.556	−0.199	−0.01	−0.016
NewTom 5G	*r*	−0.98	−0.99	−1.00	−0.99	−0.99	−0.98	−0.98	−0.98	−0.98	−0.99	−0.99	−0.98	−0.99	−0.98	−1.00
	R^2	0.94	0.91	0.97	0.98	0.97	0.93	0.99	0.96	0.97	0.93	0.93	0.92	0.98	1.00	1.00
	b	4.842	9.389	4.6036	22.483	5.9635	34.174	14.082	97.146	168.49	5.6926	26.414	9.2017	4.9247	0.1707	0.2681
	a	−1.248	−2.262	−1.214	−5.374	−1.742	−8.728	−4.006	−29.47	−41.58	−1.385	−6.426	−2.161	−1.317	−0.055	−0.089
NewTom VGi-evo	*r*	−0.99	−0.99	−0.99	−0.97	−0.99	−0.97	−0.97	−0.98	−0.97	−0.98	−0.98	−0.98	−1.00	−0.99	−1.00
	R^2	0.97	0.99	0.94	0.93	0.98	0.97	0.98	0.91	0.88	0.98	0.98	0.97	0.97	0.98	1.00
	b	11.074	7.893	5.244	24.102	7.005	57.680	24.737	130.120	274.540	9.408	43.651	14.740	7.478	0.250	0.390
	a	−3.44	−2.058	−1.436	−7.746	−2.038	−17.66	−8.453	−40.39	−73.73	−3.041	−14.11	−4.709	−2.251	−0.084	−0.134

Table 5 Upper/lower jaw (ULJ) logarithmic curve parameters for organ doses, E, and LAR incidence (males and females) for all scanners

Scanner	Parameter	Brain	Skin	Oesophagus	Eye lens	Muscles	ET	Thyroid	Salivary glands	Oral mucosa	RBM	Bone surface	Lymph nodes	ED (μSv/mAs)	LAR incidence males	LAR incidence females
Promax 3D Max	r	−0.93	−0.98	−0.99	−0.97	−0.95	−0.95	−0.99	−0.99	−0.99	−0.95	−0.95	−0.92	−0.98	−1.00	−0.99
	R^2	0.93	0.97	0.97	0.98	0.97	0.97	0.95	0.94	0.94	0.96	0.96	0.91	0.93	0.99	0.99
	b	7.608	10.221	15.288	52.738	11.398	86.413	43.669	141.050	140.370	8.819	41.091	26.279	6.984	0.247	0.467
	a	−2.147	−2.760	−3.446	−17.150	−3.462	−22.010	−11.550	−25.270	−25.370	−2.503	−11.680	−8.300	−1.495	−0.074	−0.147
Accuitomo 170	r	−0.97	−0.98	−0.99	−0.93	−0.95	−0.96	−0.99	−0.90	−0.92	−0.99	−0.99	−0.93	−0.97	−0.97	−0.97
	R^2	0.98	0.98	0.93	0.93	0.96	0.96	0.98	0.91	0.92	0.98	0.98	0.88	0.99	0.99	0.99
	b	3.177	6.600	7.117	155.740	5.150	33.292	17.862	60.474	80.756	3.931	18.241	6.473	3.422	0.116	0.229
	a	−0.678	−1.662	−1.776	−59.390	−1.387	−6.535	−4.749	−10.440	−16.590	−0.949	−4.404	−1.468	−0.744	−0.034	−0.073
CS 9300	r	−0.97	−0.99	−0.93	−0.92	−0.98	−0.94	−0.98	−0.95	−0.98	−0.99	−0.99	−0.97	−0.98	−0.99	−0.98
	R^2	0.98	0.97	0.93	0.94	0.97	0.95	0.96	0.94	0.99	0.99	0.99	0.94	0.99	0.99	1.00
	b	4.130	6.745	11.664	97.300	4.734	37.704	21.396	61.948	163.850	5.056	23.461	6.005	4.865	0.171	0.280
	a	−1.030	−1.781	−3.566	−34.430	−1.344	−7.203	−5.808	−13.330	−41.790	−1.350	−6.266	−0.145	−1.238	−0.055	−0.090
NewTom 5G	r	−0.99	−0.95	−0.96	−0.90	−0.98	−0.93	−0.95	−0.99	−0.96	−0.99	−0.99	−0.89	−0.98	−0.97	−0.97
	R^2	0.99	0.97	0.97	0.91	0.97	0.94	0.96	0.98	0.90	0.98	0.98	0.87	0.99	0.99	0.99
	b	10.139	23.645	21.517	69.492	15.632	173.240	72.584	309.070	231.870	10.047	46.620	17.704	12.937	0.455	0.840
	a	−2.118	−6.992	−5.531	−23.280	−3.332	−46.590	−21.390	−67.800	−45.840	−2.218	−10.290	−4.623	−3.155	−0.143	−0.275
NewTom VGi-evo	r	−0.96	−0.99	−0.96	−0.91	−0.95	−0.98	−0.99	−0.90	−1.00	−0.96	−0.96	−0.98	−0.96	−0.99	−0.97
	R^2	0.91	0.96	0.87	0.92	0.88	0.93	0.97	0.91	0.96	0.97	0.97	0.90	0.97	0.97	1.00
	b	30.330	18.210	13.915	60.510	22.739	162.760	73.576	389.350	363.820	20.036	92.966	28.607	16.169	0.588	0.943
	a	−8.492	−4.860	−3.070	−17.860	−7.056	−46.300	−20.840	−113.300	−77.010	−5.957	−27.640	−6.730	−4.346	−0.197	−0.309

carried out as following; Table 5 shows that the a and b factors for NewTom Vgi-evo are −113.3 and 389.35 for salivary glands and −4.346 and 16.169 for ED. Based on Eq. 1, and taking into account that $x = 8$ (the age of the patient), the normalised dose to salivary glands for this patient is 153.75 μGy/mAs and the ED is 7.13 μSv/mAs, and therefore the absolute salivary gland dose and ED values for the specific exposure (10 mAs) are 1537.5 μGy and 71.3 μSv, respectively. Apart from carrying out inter-scanner comparisons, the tabulated values in this study may also be applied to perform intra-scanner comparisons, providing guidance for optimising CBCT exposures in children.

In all cases, organ doses follow a decreasing pattern with age, as expected. The older the patient, the larger the organ, the lower the irradiated organ fraction for a given FOV, and consequently, the lower the dose. The dose decreasing pattern was verified with the Pearson correlation coefficient which in all cases was ranging between −0.9 and −1.0. Logarithmic and power fitting was attempted for organ doses, ED and LAR vs age, since it provided a coefficient of determination higher than 0.9 in all cases.

One trigger for this project was the large variability in the reported dose values in dental CBCT imaging, especially in children. A characteristic example is given in a data meta-analysis review publication by Ludlow et al [13]. The manuscript provided dose values calculated for several dental CBCT protocols with TLDs using a 10-year-old anthropomorphic phantom (ATOM, CIRS). For a small FOV acquisition (tooth imaging), there is a fivefold difference in the ED between Theodorakou et al and Ludlow et al [13, 18]. More specifically, Theodorakou et al reported an ED of 28 μSv in Accuitomo 170 for a 4×4 cm^2 FOV (90 kV, 87.5 mAs) whereas Ludlow et al reported 150 μSv for a 6×6 cm^2 FOV under the same acquisition parameters. The FOV difference cannot explain by itself the fivefold increase in the ED estimation. Furthermore, as ED dissolves any organ dose differences, a fivefold difference in ED values implies much larger differences in the estimated organ doses. For an ULJ protocol (with a FOV of 14×10 cm^2) in Accuitomo 170 (90 kV, 87.5 mAs), Theodorakou et al estimated an ED of 237 μSv whereas Ludlow et al estimated it equal to 355 μSv.

Our methodology provides an ED of 60 μSv for a CUI protocol obtained with Accuitomo 170 at 90 kV and 87.5 mAs (based on Table 4 and Eq. 1). The calculated ED is closer to Theodorakou et al rather than to Ludlow et al, given that the central upper incisors' FOV in our study is 6×6 cm^2.

For the ULJ protocol, we used a 10×10 cm^2 FOV in full accordance with the one used in clinical practice. The data in Table 5 provides an ED of 150 μSv. This value is again closer to Theodorakou et al given the difference in the size of the applied FOVs. It is essential to point out that although MC simulations provide a state-of-the-art, accurate way to calculate organ doses, the uncertainty on effective dose and life attributable risk is high due to the stochastic uncertainties on the risk coefficients. In addition, ED is not applicable to paediatric populations and does not account, without further corrections, for the gender and the age at exposure. Although LAR overcomes some of the ED limitations, LAR input risk coefficients are not available for all the radiosensitive organs in the head and neck region; these organs are included on the category of 'other cancers' when it comes to risk estimation [37]. However, both effective dose and life attributable risk were calculated in the study as they are the most commonly used and best-documented metrics for radiation-induced risk estimation. The tables also report organ doses to allow more detailed optimisation or justification studies.

Acknowledgements This work was supported by the European 415 Atomic Energy Community's Seventh Framework Programme FP7/ 416 2007–2011 under grant agreement No. 604984 (OPERRA: Open 417 Project for the European Radiation Research Area) and by the research fund of KU Leuven (OT/13/109).

Funding This work was supported by the European 415 Atomic Energy Community's Seventh Framework Programme FP7/ 416 2007–2011 under grant agreement No. 604984 (OPERRA: Open 417 Project for the European Radiation Research Area) and by the research fund of KU Leuven (OT/13/109).

Compliance with ethical standards

Guarantor The scientific guarantor is Prof. Dr. Ir. Hilde Bosmans (hilde.bosmans@uzleuven.be).

Conflict of interest The authors of this manuscript declare no relationships with any companies whose products or services may be related to the subject matter of the article.

Statistics and biometry No complex statistical methods were necessary for this paper.

Informed consent Written informed consent was not required for this study; this study was based on blind CT image datasets, not on patients themselves.

Ethical approval YES: Commissie Medische Ethiek van de Universitaire Ziekenhuizen KU Leuven, B322201525196.

Methodology
- Retrospective
- Experimental
- Multicentre study

References

1. Miracle AC, Mukherji SK (2009) Cone beam CT of the head and neck, part 2: clinical applications. AJNR Am J Neuroradiol 30: 1285–1292
2. Scarfe WC, Farman AG, Sukovic P (2006) Clinical applications of cone beam computed tomography in dental practice. J Can Dent Assoc 72:75–80

3. Carter JB, Stone JD, Clark RS, Mercer JE (2016) Applications of cone-beam computed tomography in oral and maxillofacial surgery: an overview of published indications and clinical usage in United States academic centers and oral and maxillofacial surgery practices. J Oral Maxillofac Surg 74(4):668–679
4. Pauwels R (2015) Cone beam CT for dental and maxillofacial imaging: dose matters. Radiat Prot Dosimetry 165(1–4):156–161
5. American Dental Association Council on Scientific Affairs (2012) The use of cone-beam tomography in dentistry. An advisory statement from the American Dental Association Council on Scientific Affairs. J Am Dent Assoc 143:899–902
6. European Commission (2011) Cone beam CT for dental and maxillofacial radiology: evidence based guidelines. Radiation protection publication 172. Available via http://www.sedentexct.eu/files/radiation_protection_172.pdf Last accessed 21 April 2019
7. Horner K, Islam M, Flygare L, Tsiklakis K, Whaites E (2009) Basic principles for use of dental cone beam computed tomography: consensus guidelines of the European Academy of Dental and Maxillofacial Radiology. Dentomaxillofac Radiol 38:187–195
8. Health Protection Agency (2010) Guidance on the safe use of dental cone beam CT (computed tomography) equipment HPA-CRCE-010. Chilton, Health Protection Agency
9. Jacobs R (2011) Dental cone beam CT and its justified use in oral health care. JBR-BTR 94(5):254–265
10. SEDENTEXCT Project (2011) Chapter 4, Justification and referral criteria. Surgical applications. Implant dentistry. In: Radiation protection: cone beam CT for dental and maxillofacial radiology. Evidence based guidelines 2011 (v2.0 Final)
11. Loubele M, Jacobs R, Maes F et al (2005) Radiation dose vs image quality for low-dose CT protocols of the head for maxillofacial surgery and oral implant planning. Radiat Prot Dosimetry 117(1–3):211–216
12. Stratis A, Zhang G, Lopez-Rendon X et al (2017) Two examples of indication specific radiation dose calculations in dental CBCT and multidetector CBCT scanners. Phys Med 41:71–77
13. Ludlow JB, Timothy R, Walker C et al (2015) Effective dose of dental CBCT – a meta analysis of published data and additional data for nine CBCT units. Dentomaxillofac Radiol 44:20140197
14. Pauwels R, Binsberger J, Collaert B et al (2012) Effective dose range for dental cone beam computed tomography scanners. Eur J Radiol 81:267–271
15. Ludlow JB, Ivanovic M (2008) Comparative dosimetry of dental CBCT devices and 64-slice CT for oral and maxillofacial radiology. Oral Surg Oral Med Oral Pathol Oral Radiol Endod 106:106–114
16. Rottke D, Patzelt S, Poxleitner P, Schulze D (2013) Effective dose span of ten different cone beam CT devices. Dentomaxillofac Radiol 42:20120417
17. Pauwels R, Theodorakou C, Walker A et al (2012) Dose distribution for dental cone beam CT and its implication for defining a dose index. Dentomaxillofac Radiol 41:583–593
18. Theodorakou C, Walker A, Horner K et al (2012) Estimation of paediatric organ and effective doses from dental cone beam ct using anthropomorphic phantoms. Br J Radiol 85:153–160
19. Al Najjar A, Colosi D, Dauer LT et al (2013) Comparison of adult and child equivalent doses from 2 dental cone-beam computed tomography units. Am J Orthod Dentofacial Orthop 143:784–792
20. Pauwels R, Cockmartin L, Ivanauskaité D et al (2014) Estimating cancer risk from dental cone-beam CT exposure based on skin dosimetry. Phys Med Biol 59:3877–3891
21. (2007) The 2007 recommendations of the International Commission on Radiological Protection. ICRP Publication 103. Ann ICRP 37(2–4)1–332
22. Brenner DJ (2008) Effective dose: a flawed concept that could and should be replaced. Br J Radiol 81(967):521–523
23. Martin CJ (2007) Effective dose: how should it be applied to medical exposures? Br J Radiol 80:639–647
24. Kawrakow I, Mainegra - Hing E, Rogers DW, Tessier F, Walters BRB (2009) The EGSnrc code system: Monte Carlo simulation of electron and photon transport NRCC report PIRS-701, NRC Canada. Available via https://nrc.canada.ca/en/researchdevelopment/productsservices/software-applications/egsnrc-software-tool-modelradiation-transport Last accessed 21 April 2019
25. Stratis A, Zhang G, Lopez-Rendon X, Jacobs R, Bogaerts R, Bosmans H (2016) Customization of a Monte Carlo dosimetry tool for dental cone beam CT systems. Radiat Prot Dosimetry 169(1–4):378–385
26. Zhang G, Pauwels R, Marshall N et al (2011) Development and validation of a hybrid simulation technique for cone beam CT: application to an oral imaging system. Phys Med Biol 56:5823–5843
27. Zhang G, Marshall N, Bogaerts R, Jacobs R, Bosmans H (2013) Monte Carlo modeling for dose assessment in cone beam CT for oral and maxillofacial applications. Med Phys 40:072103
28. Turner AC, Zhang D, Kim HJ et al (2009) A method to generate equivalent energy spectra and filtration models based on measurement for multidetector CT Monte Carlo simulations. Med Phys 36:2154–2164
29. Sempau J, Sanchez-Reyes A, Salvat F, Oulad ben Tahar B, Jiang SB, Fernandez-Varea JM (2001) Monte Carlo simulation of electron beams from an accelerator head using PENELOPE. Phys Med Biol 46:1163–1186
30. Walters BRB, Kawrakow I, Rogers DWO (2012) History by history statistical estimators in the beam code system. Med Phys 29:2745–2752
31. Stratis A, Touyz N, Zhang G et al (2017) Development of a paediatric head voxel model database for dosimetric applications. Br J Radiol 90(1078):20170051
32. Lee C, Lee C, Shah AP, Bolch WE (2006) An assessment of bone marrow and bone endosteum dosimetry methods for photon sources. Phys Med Biol 51:5391–5407
33. Tapiovaara M, Siiskonen T (2008) PCXMC a Monte Carlo program for calculating patient doses in medical x-ray examinations (2nd edition) STUK-A231, Edita Prima Oy, Helsinki, Finland
34. (2002) Basic anatomical and physiological data for use in radiological protection reference values. A report of age- and gender-related differences in the anatomical and physiological characteristics of reference individuals. ICRP Publication 89. Ann ICRP 32(3–4)5–265
35. Menzel HG, Clement C, DeLuca P (2009) ICRP Publication 110. Realistic reference phantoms: an ICRP/ICRU joint effort. A report of adult reference computational phantoms. Ann ICRP 39(2):1–164
36. Stratis A, Zhang G, Jacobs R, Bogaerts R, Bosmans H (2016) Rotating and translating anthropomorphic head voxel models to establish an horizontal Frankfort plane for dental CBCT Monte Carlo simulations: a dose comparison study. Phys Med Biol 61(24):N681–N696
37. National Research Council (2006) Health risks from exposure to low levels of ionizing radiation - BEIR VII. The National Academies Press, Washington, DC